the truncated topography [M. T. Zuber, D. E. Smith, *J. Geophys. Res.* **102**, 28673 (1997)]. In our approach and in earlier approaches that did not isolate the Tharsis load, the total load acting on the lithosphere consists of the topographic load plus the load necessary to account for the deformational response of the lithosphere to the imposed topographic load. Beneath Tharsis, the deformation is a depression.
11. This 95% compensation figure is an average over wavelengths corresponding to spherical harmonic degrees $l \leq 10$.
12. W. M. Folkner, C. F. Yoder, D. N. Yuan, E. M. Standish, R. A. Preston, *Science* **278**, 1749 (1997).
13. The gravity mismatch could be remedied by introducing a degree of isostatic compensation into the topography induced by the Tharsis load (*8*). Nonetheless, spatial patterns of predicted gravity anomalies and topography and how well they correlate with patterns in the observed fields are valid with the present model because the planet responds to the load only at very long wavelengths ($l \leq 10$). [D. L. Turcotte, R. J. Willemann, W. F. Haxby, J. Norberry, *J. Geophys. Res.* **86**, 3951 (1981)]. At such wavelengths, the load is supported by the resistance of the elastic shell to changes in its radius of curvature. This resistance is known as a "membrane stress." Because of membrane stress load support, plausible variations in the thickness and elastic properties of the lithospheric shell do not affect the spatial patterns of the modeled anomalies.
14. The trough may have been obscured by later deformation, evidence for which includes a series of ridges concentric to the Tharsis rise (*5*) [R. A. Schultz, K. L. Tanaka, *J. Geophys. Res.* **99**, 8371 (1994)], and by early volcanic and sedimentary deposition at the edges of the Tharsis rise (*15*).
15. D. H. Scott, K. L. Tanaka, *U.S. Geological Survey Map I-1802-A* (1986).
16. On the basis of impact crater counts, Mars has been divided into three main epochs of time; from oldest to youngest, they are the Noachian, Hesperian, and Amazonian. Assignment of absolute ages to the epoch boundaries is dependent on models for the impact flux rate. Two specific models place the Noachian-Hesperian boundary at 3.8 and 3.5 Ga and the Hesperian-Amazonian boundary at 3.55 and 1.8 Ga (*26*).
17. R. C. Anderson *et al.*, *J. Geophys. Res.*, in press.
18. Recent modeling [W. B. Banerdt, M. P. Golombek, *Lunar Planet. Sci.* **31**, abstr. 2038 (2000)] using gravity and topography fields derived from MGS observations, which are of higher degree and order than were available before, indicates that load support by bending and membrane stresses can explain the type, location, orientation, and strain of the majority of Tharsis structural features.
19. Early tectonic activity substantially predates many of the surface units of Tharsis (*15*), which typically are comparatively thin Hesperian and Amazonian deposits covering the earlier Noachian units [J. B. Plescia, R. S. Saunders, *Proc. Lunar Planet. Sci. Conf.* **11**, 2423 (1980)].
20. M. H. Carr, *Water on Mars* (Oxford Univ. Press, New York, 1996).
21. ———, *J. Geophys. Res.* **100**, 7479 (1995).
22. Azimuths were estimated from a database (*21*) consisting of almost 8000 branch segments composing over 800 valley network systems located between 47.5°N and 47.5°S. The number of valley network systems used here was reduced to 520 by eliminating systems whose downstream directions are ambiguous and by excluding valley networks that flow into the Hellas impact basin, inasmuch as their directions cannot be predicted by the model.
23. The distribution of cos δ lies between –1 and 1, with 1 meaning perfect agreement in orientation and –1 meaning that the vectors have exactly the opposite directions.
24. K. Chan, D. H. Rothman, *Phys. Rev. E*, in press.
25. B. M. Hynek, R. J. Phillips, *Geology*, in press.
26. K. L. Tanaka, D. H. Scott, R. Greeley, in *Mars*, H. H. Kieffer, B. M. Jakosky, C. W. Snyder, M. S. Matthews, Eds. (Univ. of Arizona Press, Tucson, AZ, 1992), pp. 345–382.
27. Mapped valley networks within Margaritifer Sinus (*15*, *25*) that do not have azimuths explained by the model occur almost exclusively on the same mapped unit as those that fit the model, and hence are likely to be contemporaneous. Also indicative of an equivalent age is the observation that crater densities are, within error, identical on the terrains containing network azimuths that follow and do not follow long-wavelength topography (*25*).
28. C. R. Chapman, K. L. Jones, *Annu. Rev. Earth Planet. Sci.* **5**, 515 (1977).
29. R. A. Craddock, T. A. Maxwell, *J. Geophys. Res.* **98**, 3453 (1993).
30. Horizontal layering to thicknesses of at least 8 km has been observed in the canyon walls of Valles Marineris and has been interpreted as volcanic in origin and mostly Noachian in age [A. S. McEwen, M. C. Malin, M. H. Carr, W. K. Hartmann, *Nature* **397**, 584 (1999)]. From this observation, the volcanic volume in the Valles Marineris region is estimated at $\sim 4 \times 10^7$ km^3. Because this is only a small areal fraction on a flank of the Tharsis rise, the total volume of magmatic material associated with Tharsis overall must be approximately an order of magnitude larger, which is consistent with our model results.
31. T. M. Gerlach, E. J. Graber, *Nature* **313**, 273 (1985).
32. H. Y. McSween Jr. *et al.*, *Nature* **409**, 487 (2001).
33. F. Forget, R. T. Pierrehumbert, *Science* **278**, 1273 (1997).
34. D. A. Brain, B. M. Jakosky, *J. Geophys. Res.* **103**, 22 (1998).
35. M. H. Carr, *J. Geophys. Res.* **104**, 21 (1999).
36. We thank the MGS Radio Science and the Mars Orbiter Laser Altimeter (MOLA) investigations, which are supported by the NASA Mars Exploration Program.

29 December 2000; accepted 2 March 2001
Published online 15 March 2001;
10.1126/science.1058701
Include this information when citing this paper.

Role of the Stratospheric Polar Freezing Belt in Denitrification

A. Tabazadeh,[1]* E. J. Jensen,[1] O. B. Toon,[2] K. Drdla,[1] M. R. Schoeberl[3]

Homogeneous freezing of nitric acid hydrate particles can produce a polar freezing belt in either hemisphere that can cause denitrification. Computed denitrification profiles for one Antarctic and two Arctic cold winters are presented. The vertical range over which denitrification occurs is normally quite deep in the Antarctic but limited in the Arctic. A 4 kelvin decrease in the temperature of the Arctic stratosphere due to anthropogenic and/or natural effects can trigger the occurrence of widespread severe denitrification. Ozone loss is amplified in a denitrified stratosphere, so the effects of falling temperatures in promoting denitrification must be considered in assessment studies of ozone recovery trends.

Polar stratospheric cloud (PSC) sightings date back to the 19th century (*1*). Up to a few decades ago, PSCs were known primarily for their colorful glows that occasionally filled up the skies over the poles in winter and early spring. Soon after the discovery of the springtime Antarctic "ozone hole" (*2*), chlorofluorocarbons (CFCs) (*3*) along with naturally occurring PSCs (*4*) were identified as important agents in ozone destruction. It was hypothesized (*4*) and later proven (*5*, *6*) that PSCs promote formation of active chlorine, originally derived from man-made emission of CFCs (*3*), that catalytically destroys ozone molecules.

Another interesting feature of some PSCs is that they contain large amounts of nitric acid (*7*, *8*). Recent analysis of space-borne observations (*9*) indicates that a continuous downward flow of large cloud particles (larger than a few micrometers) can form within persistent PSCs. This flux of large particles can remove a substantial amount of nitric acid from the altitude range in which PSCs can form (~16 to 24 km) in periods of less than 2 weeks (*9*). The process of irreversible nitric acid removal from the stratosphere is known as denitrification (*7*, *10*, *11*). Currently, it occurs extensively only inside the Antarctic vortex (*9*, *12*). A denitrified stratosphere in early spring is primed for ozone destruction because reactive nitrogen that can mediate ozone loss (by sequestering active chlorine) has been removed from the stratosphere (*13*).

Even after more than a decade of research on PSCs, a quantitative understanding of how large nitric acid–containing cloud particles (*14*) form in the stratosphere has remained elusive (*13*, *15*). Many in situ and remote sensing observations show the existence of both small liquid and large solid cloud particles containing nitric acid in the polar stratosphere (*13*, *16*). Liquid nitric acid–containing cloud particles are composed of supercooled ternary solutions (STS) of nitric acid, sulfuric acid, and water (*17*, *18*). Because STS particles form by condensational growth, their

[1]NASA Ames Research Center, Earth Science Division, MS:245-4 Moffett Field, CA 94035, USA. [2]Laboratory for Atmospheric and Space Physics, Program in Atmospheric and Oceanic Sciences, University of Colorado, Boulder, CO 80309, USA. [3]NASA Goddard Space Flight Center, Greenbelt, MD 20771, USA.

*To whom correspondence should be addressed. E-mail: atabazadeh@mail.arc.nasa.gov

average size remains below 0.5 μm, making them inefficient in denitrifying the stratosphere. Several theories (*13*) have been put forward to explain how large nitric acid di- and trihydrate (NAD and NAT) particles selectively nucleate and grow in the stratosphere (*14*). However, all reported studies (*13*) lack a quantitative description of the underlying nucleation processes involved.

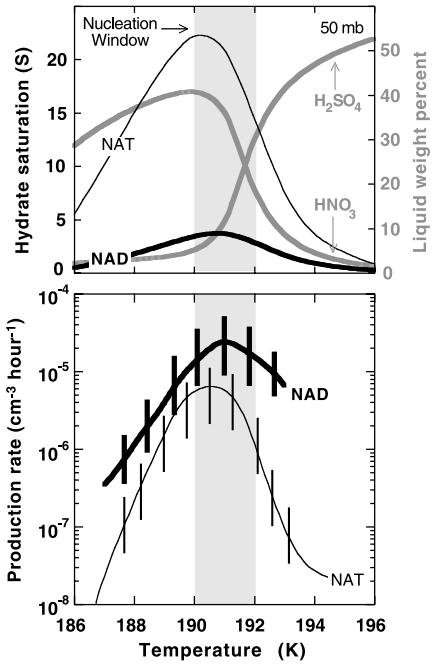

Fig. 1. APCM calculations of STS composition and hydrate saturation in solution as a function of temperature. For a given temperature, the hydrate saturation in solution is computed by dividing the vapor pressure of HNO_3 over an STS solution (calculated from the APCM) by the computed vapor pressure of HNO_3 over NAD (*37*) and NAT phases (*39*). In the lower panel, temperature-dependent hourly hydrate particle production rates for an assumed size distribution of background aerosols [number density N = 15 cm^{-3}, σ = 1.8, and diameter = 1.82 μm (*40*)] are shown. Vertical bars show the sensitivity of hydrate particle production rates to *J* uncertainties (*21, 27*). Calculations were performed at 50 mbar (~20 km) for HNO_3, H_2O, and H_2O_4 mixing ratios of 9 ppbv, 5 parts per million by volume (ppmv), and 0.5 ppbv, respectively.

We have incorporated rate equations describing the homogeneous freezing rates of NAD and NAT from STS (*19–21*) into a one-dimensional (1D) cloud model (*22*) to simulate the formation, growth, and sedimentation of large NAD and NAT particles. STS properties in solution are calculated using an aerosol physical chemistry model (APCM) (*17*). APCM results are read into the 1D Community Aerosol Radiation Model for the Atmosphere (CARMA) that treats growth and sedimentation, which determine the magnitude and the depth of the denitrification for a given set of known atmospheric conditions. The CARMA model has been validated and successfully applied to study the properties of both cirrus (*23*) and PSCs (*11*).

Figure 1 shows STS composition and hydrate saturation (S) variations with temperature at 50 mbar. The NAD and NAT S ratios were used to calculate hydrate particle production rates in the atmosphere. The narrow temperature margin centered around 191 K (to within ±1 K), where NAD particle production rates peak in solution is refereed to as the "nucleation window" (*24*). On average, the hourly NAD (NAT) particle production rate in an air mass traveling within the nucleation window is about 2×10^{-5} (4×10^{-6}) cm^{-3}. Once an air mass exits the nucleation window, hydrate particle production rates drop quickly, particularly at the low-temperature end (Fig. 1). Thus, homogeneous freezing of solid PSCs occurs more readily in air masses that are cooling slowly because such air masses have a better chance of being exposed to optimal freezing temperatures for longer periods than those cooling at a faster rate.

In Fig. 2, the time evolution of the area enclosed by the nucleation window (Fig. 1) is shown for three polar winters. Polar projection maps are shown for 3 days to visualize how the margins of the nucleation window spatially transform into an area that encircles the polar vortex. We refer to this optimal freezing area as a "polar freezing belt." In the Antarctic, the polar freezing belt is persistent for over 3 months, whereas for the cold Arctic winters studied here, the polar freezing belt is present for approximately a month. However, when present, the freezing areas are comparable in size over both hemispheres and are 1/4 to 3/4 as large as the size of the continental United States. Hence, the freezing areas are spatially large, and the polar freezing belt thus can act as an efficient engine to produce continuously solid PSC particles inside the polar vortex. The major difference between the two poles at present is the size of the NAD stability areas (Fig. 2, areas with temperatures <192 K) in which nucleated NAD particles can grow to become large particles (*14*). In the Antarctic, NAD stability areas are two to three times larger than those in the Arctic, resulting in the formation of more persistent clouds (*9*) that can lead to severe denitrification.

Double-headed arrows in Fig. 2 mark the study periods during which solid PSC properties were calculated. The Antarctic study period is chosen because denitrification is actively occurring during this time (*9*). The Arctic study periods are selected because they present the coldest 4-week period during which PSC lifetimes are most Antarctic-like in duration (*9*). PSC lifetimes computed for the 1999–2000 Arctic winter study period are, on the average, 2 to 3 days longer than those calculated previously (*9*) for a few cold Arctic winters in the 1990s. The effect of longer lasting PSCs during the last Arctic winter in promoting denitrification is discussed here.

Computed (*25*) nitric acid hydrate cloud properties, which are in good agreement with recent in situ measurements of large HNO_3-containing cloud particles during the 1999–2000 Arctic winter (*26*), are similar over both poles (Fig. 3). For standard runs (*27*), NAD is the dominant hydrate in the column for most altitudes. The uncertainties in *J* values (*27*) result in large variations in NAD number densities (factors of 2 to 10) but not NAD particle sizes (horizontal bars in Fig. 3). For nearly all altitudes, NAT particles are larger than NAD. When NAD is converted to NAT (*28*), NAT number densities increase by nearly an order of magnitude relative to values found from NAT nucleating directly from STS (*27*), whereas NAT particle sizes are not greatly affected (Fig. 3).

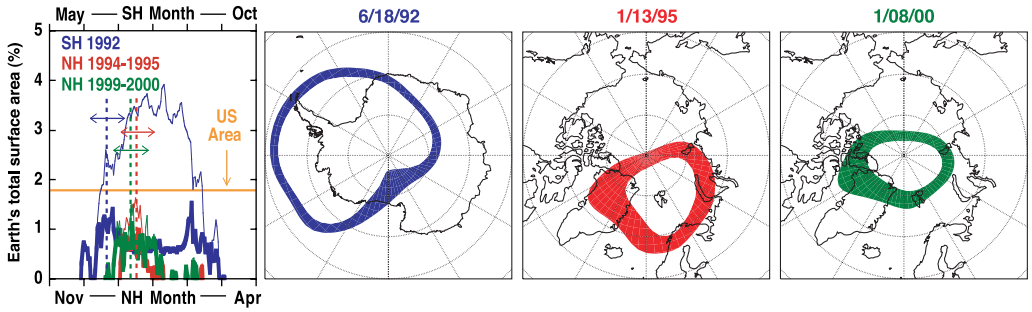

Fig. 2. Time evolution of cold areas for one Antarctic (SH) and two Arctic (NH) winters at 50 mbar (~20 km). The thin and thick lines show total areas below 192 K and between 190 and 192 K, respectively. The thin lines also show roughly the areas in which NAD particles were stable in the atmosphere (*37*). Parcel initialization dates (*25*) for each winter are marked as vertical dashed lines (18 June 1992, 13 January 1995, and 8 January 2000), and their corresponding polar projection maps are also shown. Colored belts show the spatial coverage of areas between 190 and 192 K temperature contours. Double-headed arrows mark the periods (±2 weeks from the marked initialization dates) during which model calculations were performed (*22, 25*).

Final HNO_3 profiles for different assumptions of *J* values and particle types are shown in Fig. 4 (*27*, *28*). Low particle number densities shown in Fig. 3 resulted in substantial denitrification in some air parcels, except when lower-bound *J* values (*27*) are used in the model. Because lidar (*16*) and in situ studies (*26*) show that large PSC particles are widespread in the Arctic, the lower-bound *J* values (*27*) are not appropriate for atmospheric applications if homogeneous freezing is to explain large solid particle observations in the Arctic. Results from standard and upper-bound *J* values (*27*) indicate that denitrification is primarily caused by sedimentation of 4- to 7-μm NAD particles [containing ~1 to 2 parts per billion by volume (ppbv) of condensed phase HNO_3 in cm^{-3} of air] and that larger NAT particles (containing less than 0.3 ppbv of condensed phase HNO_3 in cm^{-3} of air) contribute to at most 10% of the overall denitrification. When NAD is converted to NAT (*28*), denitrification is significantly enhanced (Fig. 4) compared with standard results (*27*).

Figure 4 shows a near-complete depletion of Antarctic nitric acid profiles after 4 weeks of simulation (*29*). Arctic profiles are less depleted and the depth of the column is not as deep as that computed for the Antarctic, even for the 1999–2000 winter that has been shown to be the coldest Arctic winter over the last two decades (*30*). However, for standard results (*27*) all nitric acid profiles for the 1999–2000 winter (green horizontal bars in Fig. 4) show some degree of denitrification (~20 to 55% nitric acid depletion at the peak height of the denitrified layers at ~21 km). In contrast, the 1994–1995 Arctic winter still does not show the development of a distinct denitrification profile, even with model assumptions that maximize hydrate particle production rates. We attribute the growth in the depth of the denitrified layers in the last Arctic winter to the presence of unusually long lasting PSCs in the early part of January.

Denitrified layer computed depths (*25*) are compared against the nitric acid vertical resolution of the MLS (Microwave Limb Sounder) (~6 km) and ILAS (Improved Limb Atmospheric Spectrometer) (~1 km) instruments onboard the UARS (Upper Atmosphere Research Satellite) and ADEOS (Advanced Earth Observing Satellite) satellites, respectively (Fig. 4). Because Arctic (not Antarctic) denitrified layers are shallow in depth, MLS (*12*, *31*) is unable to detect measurable HNO_3 redistribution within these layers. However, the ILAS (*32*) has recorded ~40% de- and renitrification in cold Arctic air parcels (Fig. 4). For both Arctic winters studied here, the calculated de- and renitrification that occurred in the model is precisely observable by the ILAS but not by the MLS. In addition, the growth in the depth of denitrified layers calculated here for the 1999–2000 winter could be the main reason why MLS has seen for the first time evidence of widespread Arctic denitrification on the order of ~20% (*31*). Thus, model calculations presented here are consistent with space-borne observations of nitric acid loss over both poles during the last decade. Also, Arctic HNO_3 profiles in Fig. 4 show large perturbations in the HNO_3 concentration around the ER-2 aircraft cruise altitude (~18 to 20 km). This could explain why many in-situ gas phase HNO_3 measurements (*13*, *26*, *33*) during past cold Arctic winters show evidence of over 50% denitrification at the ER-2 cruise altitude.

Currently the thermal structure of the Arctic (*11*) is such that PSCs are relatively short-lived (*9*), which (as we show here) limits the possible vertical range of denitrification to a few kilometers in most Arctic air parcels. However, with a growing trend in the concentration of greenhouse gases, the lower stratosphere is predicted to become colder in the future (*13*, *34*). In Fig. 4 the computed magnitude of denitrification is greatly enhanced for the 1999–2000 Arctic winter when vertical temperature profiles used in the model (*22*, *25*) are cooled by 4 K (*9*). To cause such a dramatic cooling in the Arctic, a major contribution from currently not-well-understood dynamical factors would be required because the direct radiative cooling due to the greenhouse gas buildup can only cool the stratosphere by about 1 to 2 K over the next two decades (*34*).

Severity in the growth of denitrification due to future colder polar temperatures can delay the recovery of Arctic ozone if climate change and/or natural variability can significantly affect the thermal structure of the Arctic in the coming decades. Also, the future occurrence of denitrification in the colder boundaries of the Antarctic vortex edge can

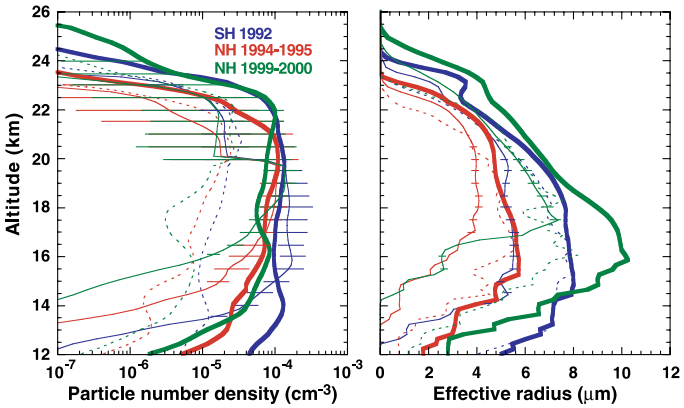

Fig. 3. Average NAD (thin lines) and NAT (dashed lines) particle size and number density after 2 weeks of simulation. The curves are obtained by averaging at each altitude the size and number density variations calculated in all parcels (*25*). The thin solid and dashed lines are calculated using standard *J* values (*27*). The horizontal bars show the sensitivity of NAD particle size and number density to *J* uncertainties (*27*). The thick lines show NAT cloud properties when NAD is converted to NAT (*28*).

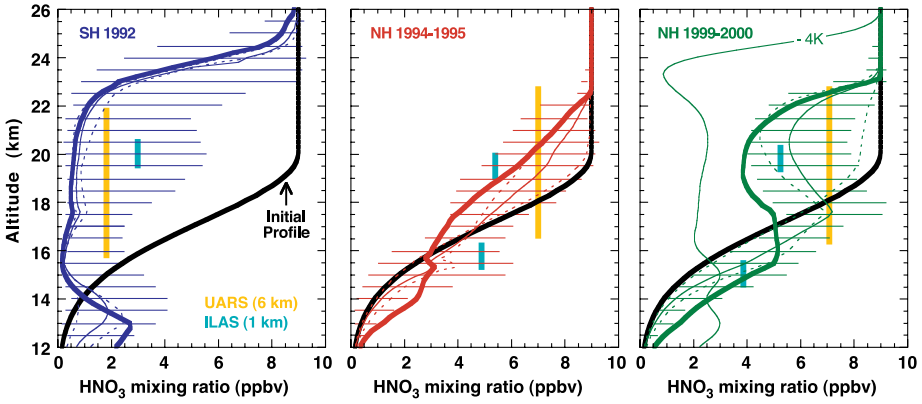

Fig. 4. Final average HNO_3 mixing ratio profiles after 4 weeks of simulation. Thin solid lines are calculated using standard *J* values (*27*), and the effect of *J* uncertainties on the results are shown as dashed lines (*27*). The thick lines show final HNO_3 mixing ratios when NAD is converted to NAT (*28*). The lines are obtained by averaging at each altitude the HNO_3 mixing ratio variations in all parcels (*25*). The range of variation in HNO_3 mixing in all parcels for standard *J* values (*27*) are shown as horizontal bars. The thin solid green line (labeled as −4 K) shows the standard (*27*) shift in the average denitrification profile for the 1999–2000 winter when parcel vertical temperature profiles are lowered by 4 K in the model (*22*, *25*). The blue and gold vertical bars show the vertical resolution of the UARS MLS and ILAS instruments, respectively. The ILAS bars also mark the altitude ranges where the instrument has observed up to 40% de- and renitrification in the Arctic (*32*).

cause the area of the Antarctic "ozone hole" to spread beyond those measured in the 1990s. Thus, the effect of denitrification on ozone recovery in both hemispheres cannot be ignored and must be included quantitatively in assessment models for better predictions of future springtime polar ozone trends.

References and Notes

1. J. L. Stanford, J. S. Davis, *Bull. Am. Meteorol. Soc.* **55**, 213 (1974).
2. J. C. Farman, B. G. Gardiner, J. D. Shanklin, *Nature* **315**, 207 (1985).
3. M. J. Molina, F. S. Rowland, *Nature* **249**, 820 (1974).
4. S. Solomon, R. R. Garcia, F. S. Rowland, D. J. Wuebbles, *Nature* **321**, 755 (1986).
5. M. J. Molina, T-L. Tso, L. T. Molina, F. C. Y. Wang, *Science* **238**, 1253 (1987).
6. M. A. Tolbert, M. J. Rossi, R. Malhotra, D. M. Golden, *Science* **238**, 1258 (1987).
7. O. B. Toon, P. Hamill, R. P. Turco, J. Pinto, *Geophys. Res. Lett.* **13,** 1284 (1986).
8. P. J. Crutzen, F. Arnold, *Nature* **324**, 651 (1986).
9. A. Tabazadeh *et al.*, *Science* **288**, 1407 (2000).
10. R. J. Salawitch, G. P. Gobbi, S. C. Wofsy, M. B. McElroy, *Nature* **339**, 525 (1989).
11. O. B. Toon, R. P. Turco, P. Hamill, *Geophys. Res. Lett.* **17**, 445 (1990).
12. M. L. Santee, G. L. Manney, L. Froidevaux, W. G. Read, J. Waters, *J. Geophys. Res.* **104**, 8225 (1999).
13. *WMO Scientific Assessment of Ozone Depletion: 1998, Rep. 44* (1999), chapter 3.
14. Selective nucleation of just a few STS particles into more stable crystalline forms of nitric acid sets the stage for the differential growth process (*10*, *11*), which results in the occurrence of a very small population of relatively large nitric acid hydrate cloud particles. It is the sedimentation of these large nitric acid hydrate particles that leads to denitrification.
15. M. A. Tolbert, *Science* **272**, 1597 (1996).
16. O. B. Toon, A. Tabazadeh, E. V. Browell, J. Jordan, *J. Geophys. Res.* **105**, 20589, (2000).
17. A. Tabazadeh, R. P. Turco, K. Drdla, M. Z. Jacobson, O. B. Toon, *Geophy. Res. Lett.* **21**, 1619 (1994).
18. K. S. Carslaw, B. P. Luo, S. L. Clegg, T. Peter, P. Brimblecombe, P. Crutzen, *Geophys. Res. Lett.* **21**, 2479 (1994).
19. A. K. Bertram, D. B. Dickens, J. J. Sloan, *J. Geophys. Res.* **105**, 9283 (2000).
20. D. Salcedo, L. T. Molina, M. J. Molina, *J. Phys. Chem.* **105**, 1433 (2001).
21. The results of laboratory freezing rates are parameterized into simple functions of the form (*20*)

$$J_{NAD} = 1.138 \times 10^{34}\sqrt{T}r^3 \exp\left[\frac{-\Delta G_{act}^{NAD}}{RT}\right],$$

where

$$\Delta G_{act}^{NAD} = (28.8 \pm 0.2) - (0.37 \pm 0.01)S_{NAD}$$

$$J_{NAT} = 9.269 \times 10^{33}\sqrt{T}r^3 \exp\left[\frac{-\Delta G_{act}^{NAT}}{RT}\right],$$

where

$$\Delta G_{act}^{NAT} = (30.9 \pm 0.3) - (0.14 \pm 0.0004)S_{NAT}$$

where J is the freezing rate of a single particle in sec^{-1}, T is temperature in K, r is the particle radius in cm, ΔG_{act} is the activation free energy for the formation of hydrate germs in solution in units of kcal mol^{-1} (*20*), S is hydrate saturation in solution, and R is the universal ideal gas constant in units of kcal mol^{-1} K^{-1}. To account for the effect of particle size on freezing, we have slightly modified (*35*) the pre-exponential factor from that given in Salcedo *et al.* (*20*).
22. The 1D model uses vertical temperature profiles that are constructed using the archived NASA Goddard National Centers for Environmental Prediction (NCEP) data (*36*). To obtain a vertical temperature profile, a single position is first selected on the 450 K surface (~50 mbar) inside a cloudy region ($T < 192$ K). Next, air parcel trajectories (*36*) are run forward and backward for 2 weeks from the chosen location to obtain a 4-week-long temperature and position history of an air parcel. Positions along the 4-week-long trajectory at the 450 K level are used to read off vertical temperature profiles at each location and time along the parcel's path using the NCEP data.
23. E. J. Jensen, O. B. Toon, D. L. Westphal, S. Kinne, A. J. Heymsfield, *J. Geophys. Res.* **99**, 10443 (1994).
24. Cloud model sensitivity studies (*22*) indicate that hourly NAD and/or NAT hydrate particle production rates $<\sim 10^{-5}$ cm^{-3} (Fig. 1) can result in 10% denitrification at most in typical air parcels before particle evaporation occurs. Thus, NAD particle production within the nucleation window is the dominant process that controls the overall atmospheric number density of the nitric acid hydrated particles. Direct NAT particle production rate from STS is $<10^{-5}$ cm^{-3} in the atmosphere (Fig. 1), making this process unimportant to denitrification. The temperature margins of the nucleation window vary as a function of total pressure, H_2O mixing ratio, and HNO_3 mixing ratio.
25. To compute cloud microphysical properties, 20 initial points were homogeneously distributed within the 192 K temperature contour at 50 mbar for the 3 days marked as dashed lines in Fig. 2. These days represent cloudy conditions in the middle of each study period (marked as bounded arrows in Fig. 2). We ran trajectories forward and backward from each initialized point to obtain 20 4-week-long air parcel temperature histories for each winter; their corresponding vertical temperature profiles are constructed as described above (*22*).
26. D. W. Fahey *et al.*, *Science* **291**, 1026 (2001).
27. For standard model runs, mean ΔG values were used in the J expressions for both NAD and NAT (*21*). Sensitivity studies were also performed by using upper and lower limits for ΔG in the J expressions for both hydrates.
28. To account for NAD to NAT conversion in the model, the assumptions were used for J values as follows: J_{NAT} = standard J_{NAD} + standard J_{NAT} and $J_{NAD} = 0$ (*27*). Most laboratory observations indicate that the metastable NAD phase is the nucleus that initially forms in aerosol particles (*13*, *19*, *20*, *37*). In general, kinetically favorable phases usually nucleate first in particles, and in time such metastable phases often but not always transition into the most stable form (*37*). Thus, the possibility of NAD to NAT conversion in the atmosphere is likely, and recent in situ NAT particle observations (*38*) seem to support this hypothesis.
29. Due to cold temperatures roughly 1 to 4 ppbv of HNO_3 between 17 to 23 km is sequestered in the STS phase at the end of the Antarctic calculations in most air parcels. The STS content is sensitive to both J uncertainties (*27*) and the assumption of NAD to NAT conversion (*28*).
30. G. L. Manney, J. L. Sabutis, *Geophys. Res. Lett.* **27**, 2589 (2000).
31. M. L. Santee, G. L. Manney, N. J. Livesey, J. W. Waters, *Geophys. Res. Lett.* **27**, 3213 (2000).
32. Y. Kondo, H. Irie, M. Koike, G. E. Bodeker, *Geophys. Res. Lett.* **27**, 337 (2000).
33. H. J. Hintsa, *Geophys. Res. Lett.*, **25**, 501 (1998).
34. D. T. Shindell, D. Rind, P. Lonergan, *Nature*, **392**, 589 (1998).
35. A. Tabazadeh, S. T. Martin, J. S. Lin, *Geophys. Res. Lett.* **27**, 1111 (2000).
36. M. R. Schoeberl, S. Doiron, L. R. Lait, P. A. Newman, A. J. Krueger, *J. Geophys. Res.* **98**, 2949 (1992).
37. D. R. Worsnop, L. E. Fox, M. S. Zahniser, S. C. Wofsy, *Science* **259**, 71 (1993).
38. C. Voigt *et al.*, *Science* **290**, 1756 (2000).
39. D. R. Hanson, K. Mauersberger, *Geophys. Res. Lett.* **15**, 855 (1988).
40. J. E. Dye *et al.*, *J. Geophys. Res.* **97**, 8015 (1992).

41. We are grateful to D. Salcedo for providing us with preprint copies of her paper and thesis on stratospheric aerosol freezing. We thank M. Santee, N. Larsen, P. Hamill, and A. Ackerman for helpful comments and suggestions. Supported by two separate NASA programs, the Upper Atmosphere Research Satellite (UARS) and the Atmospheric Chemistry Modeling and Analysis Program (ACMAP). A.T. also acknowledges support from a Presidential Early Career Award for Scientists and Engineers.

7 November 2000; accepted 28 February 2001

Biospheric Primary Production During an ENSO Transition

Michael J. Behrenfeld,[1]* James T. Randerson,[2] Charles R. McClain,[1] Gene C. Feldman,[1] Sietse O. Los,[3] Compton J. Tucker,[1] Paul G. Falkowski,[4] Christopher B. Field,[5] Robert Frouin,[6] Wayne E. Esaias,[1] Dorota D. Kolber,[4] Nathan H. Pollack[7]

The Sea-viewing Wide Field-of-view Sensor (SeaWiFS) provides global monthly measurements of both oceanic phytoplankton chlorophyll biomass and light harvesting by land plants. These measurements allowed the comparison of simultaneous ocean and land net primary production (NPP) responses to a major El Niño to La Niña transition. Between September 1997 and August 2000, biospheric NPP varied by 6 petagrams of carbon per year (from 111 to 117 petagrams of carbon per year). Increases in ocean NPP were pronounced in tropical regions where El Niño–Southern Oscillation (ENSO) impacts on upwelling and nutrient availability were greatest. Globally, land NPP did not exhibit a clear ENSO response, although regional changes were substantial.

Temporal changes in the physical environment are manifested in the light-harvesting capacity of plant communities throughout the biosphere and can be monitored remotely by changes in surface chlorophyll concentration (C_{sat}) in the oceans and the Normalized Difference Vegetation Index (NDVI) on land. A continuous, 20-year global record of satellite NDVI has permitted characterization of interannual, climate-driven changes in terrestrial photosynthesis (*1*–*5*). Coincident changes in ocean productivity have not been assessed because an analogous long-term global C_{sat} record does not exist. The first C_{sat} measure-